

Influence of lake-basin morphology on climate-sediment transfer functions: Early Eocene Wilkins Peak Member, Green River Formation, Wyoming

Andrew P. Walters^{1,†}, Alan R. Carroll¹, Stephen R. Meyers¹, and Tim K. Lowenstein²

¹Department of Geoscience, University of Wisconsin–Madison, 1215 West Dayton Street, Madison, Wisconsin 53706, USA ²Department of Geological Sciences and Environmental Studies, Binghamton University, Binghamton, New York 13902, USA

ABSTRACT

Lacustrine strata are often among the highest-resolution terrestrial paleoclimate archives available. The manner in which climate signals are registered into lacustrine deposits varies, however, as a function of complex sedimentologic and diagenetic processes. The retrieval of reliable records of climatic forcing therefore requires a means of evaluating the potential influence of changing sedimentary transfer functions. Here, we use high-resolution X-ray fluorescence core scanning of the Wilkins Peak Member of the Green River Formation to characterize the long-term evolution of transfer functions in an ancient lacustrine record.

Our analysis identifies a shift in the frequency distribution of Milankovitch-band variance between the lower and middle Wilkins Peak Member across a range of temporally calibrated elemental intensity records. Spectral analysis of the lower Wilkins Peak Member shows strong short eccentricity, obliquity, precession, and sub-Milankovitch-scale variability, while the middle Wilkins Peak Member shows strong eccentricity variability and reduced power at higher frequencies. This transition coincides with a dramatic decline in the number and volume of evaporite beds.

We attribute this shift to a change in the Wilkins Peak Member depositional transfer function caused by evolving basin morphology, which directly influenced the preservation of bedded evaporite as the paleolake developed from a deeper, meromictic lake to a shallower, holomictic lake. The loss of bedded evaporite, combined with secondary evapo-

†Present address: Department of Geosciences, University of Arizona, 1040 East 4th Street, Tucson, Arizona 85721, USA; apwalters@arizona.edu. rite growth, results in reduced obliquityand precession-band power and enhanced eccentricity-band power in the stratigraphic record. These results underscore the need for careful integration of basin and depositional system history with cyclostratigraphic interpretation of the dominant astronomical signals preserved in the stratigraphic archive.

INTRODUCTION

Lacustrine deposits are among the most valuable geological archives of terrestrial sedimentary deposition and offer a detailed and integrative perspective on continental variation in climate, tectonics, landscape evolution, and ecology. Changes in physical, chemical, and biological processes within a lake and its associated watershed are particularly useful in understanding influences on continental environments in deep time, especially during periods of major climatic, tectonic, or biologic change (e.g., Surdam and Stanley, 1980; Johnson, 1984; Hendrix et al., 1992; Mingram, 1998; Pietras et al., 2003a, 2003b; Cohen et al., 2007; Smith et al., 2008; Carroll et al., 2010; Smith et al., 2014a, 2014b; Bernhart Owen et al., 2019).

However, it has long been recognized that not all lakes are equally sensitive recorders of environmental change, with some lacustrine systems amplifying, muting, or selectively filtering the environmental signals preserved in their depositional records (Hutchinson, 1957; Cohen, 2003). This variable sensitivity to environmental forcing may be thought of as differences in the depositional "transfer function," a term that describes the process by which an environmental signal is quantitatively encrypted into the geologic record through climatic, depositional, burial, and diagenetic processes (Meyers et al., 2008; Zeebe et al., 2017). Whereas the depositional transfer function plays a key role in filtering how environmental signals are preserved in the sedimentary record, its influence on the geological record of deep-time paleolakes is not well understood.

The Wilkins Peak Member of the Green River Formation in Wyoming (Fig. 1) represents one of the premier lacustrine records of the early Eocene, and it makes a compelling deep-time locale from which to study the long-term evolution of depositional transfer functions. Not only does the Wilkins Peak Member have a thick, temporally well-constrained, and highly studied foreland basin record of lacustrine and alluvial deposition during the early Eocene climatic optimum greenhouse climate (EECO; 52–50 Ma; Zachos et al., 2001, 2008; Smith et al., 2003, 2008), but the Green River Formation-including the Wilkins Peak Member-also has a long history of cyclostratigraphic study, including the interpretation of a range of Milankovitchand sub-Milankovitch-scale cyclicity (Bradley, 1929; Fischer and Roberts, 1991; Pietras et al., 2003a; Machlus et al., 2008; Meyers, 2008; Aswasereelert et al., 2013; Dyer-Pietras, 2020).

This study aims to evaluate the evolution of the Wilkins Peak Member depositional transfer function through the development of a highresolution, multi-element X-ray fluorescence core-scanning data set. This data set was temporally calibrated using radioisotopic ages of intercalated tuff horizons (Smith et al., 2003, 2008, 2010; Machlus et al., 2015), which eliminated the need for astronomical tuning. Spectral analysis of this new data set allows us to characterize cyclic sedimentation within the Wilkins Peak Member at a previously unattainable level of detail to assess changes in the expression of cyclic sedimentation and evaluate potential transfer-function linkages to climate, tectonics, and landscape evolution.

GEOLOGIC SETTING

The Green River Formation was deposited in a series of mid-latitude, Laramide foreland

published online 9 February 2023

GSA Bulletin;

https://doi.org/10.1130/B36566.1; 10 figures; 3 tables; 1 supplemental file.

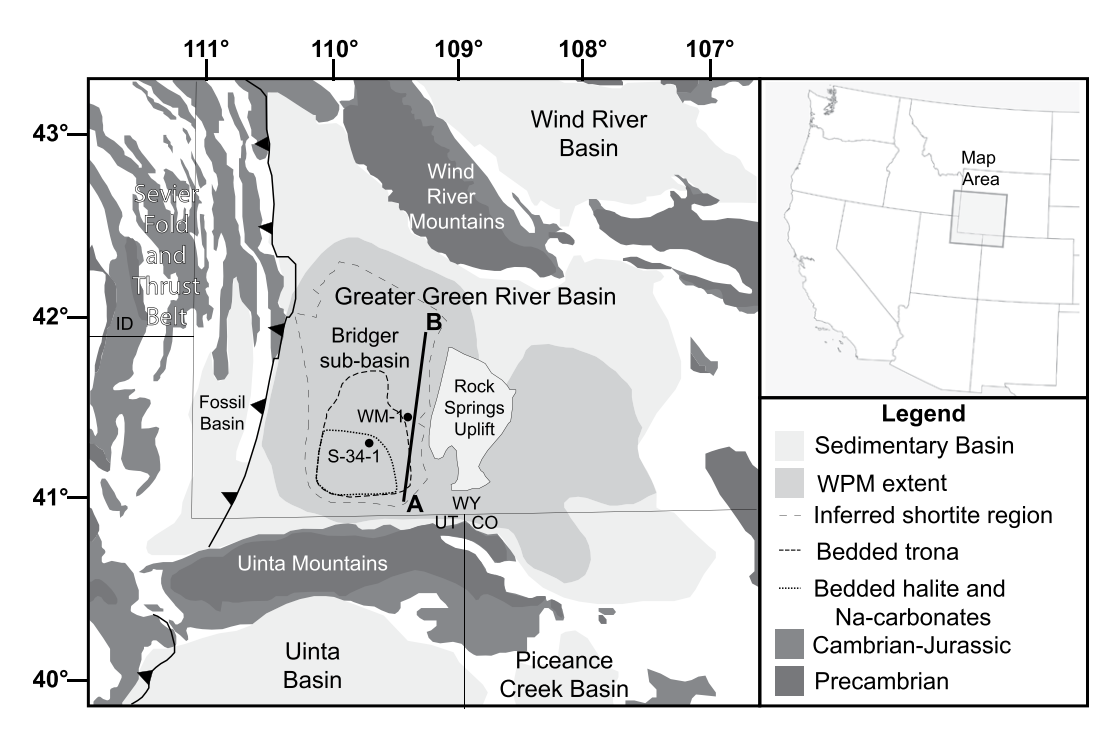


Figure 1. Location map shows the Greater Green River Basin, Green River Formation. The Solvay S-34-1 core is located at 41.414231°N, 109.69675°W (WGS 84). Modified from Smith et al. (2008) and Jagniecki and Lowenstein (2015). WPM—Wilkins Peak Member.

basins during the early to middle Eocene (ca. 54-43 Ma; Smith et al., 2008, 2010) (Figs. 1 and 2). Sedimentary deposition in this regional lacustrine system was centered around four primary basins: the Greater Green River Basin (southwestern Wyoming), the Fossil Basin (southwestern Wyoming), the Uinta Basin (northeastern Utah), and the Piceance Creek Basin (northwestern Colorado). This study focuses on the western portion of the Greater Green River Basin, termed the Bridger subbasin. This sub-basin is bounded in the south by the Uinta Mountains, in the west by the Sevier fold and thrust belt, in the east by the Rock Springs Uplift, and in the north by the Wind River Mountains (Fig. 1). Broad and low in relief in comparison to the other Green River Formation basins, it contains a thick sequence of strata deposited in Lake Gosiute and its associated alluvial deposits.

Broadly, the Green River Formation in the Bridger sub-basin is divided into four primary depositional members. In ascending order, they are the Luman Tongue, the Tipton Member, the Wilkins Peak Member, and the Laney Member (Fig. 2). This study evaluates the Wilkins Peak Member, which was deposited in an underfilled lake with persistent, widespread alkaline and hypersaline conditions (Eugster and Hardie, 1975; Smoot, 1983; Carroll and Bohacs, 1999; Pietras and Carroll, 2006; Smith et al., 2015). Deposition of this unit (ca. 51.5–50 Ma) is also partly coincident with the early Eocene climatic optimum (EECO; ca. 53–50 Ma), the peak of the early Cenozoic greenhouse climate interval

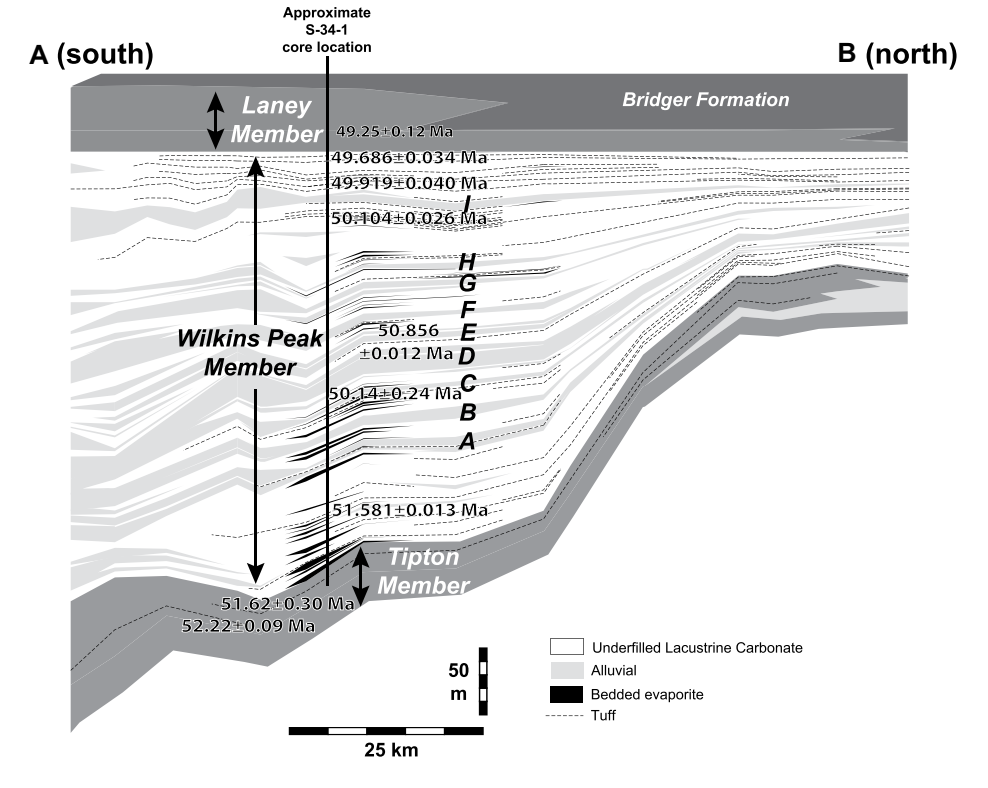


Figure 2. Image shows the cross section of the Bridger sub-basin, Greater Green River Basin, across the A–B transect shown in Figure 1. Within the Wilkins Peak Member, 25 major evaporite beds have been identified, correlated within the basin, and assigned numerical designations (trona beds 1–25) (Wiig et al., 1995). Additionally, nine major alluvial marker beds, designated A–I, have been identified and correlated within the basin. Note that the Luman Tongue is limited in extent to the southern margin of the basin and is not shown on this cross section. Radioisotopic ages are from Smith et al. (2008, 2010) and Machlus et al. (2015). Modified from Smith et al. (2015).

(Zachos et al., 2001, 2008; Smith et al., 2008). Shallow lake levels, combined with the broad, low-relief morphology of the basin, appear to have made this unit particularly sensitive to climatic forcing—including hypothesized astronomical cycles—over this unusually warm period (Fischer and Roberts, 1991; Machlus et al., 2008; Meyers, 2008; Aswasereelert et al., 2013).

The Wilkins Peak Member ranges from 200 m thick to 325 m thick in the depocenter of the Bridger sub-basin and is dominantly composed of lacustrine marlstone, lacustrine bedded and displacive evaporite, and alluvial siliciclastic deposits (Fig. 2). Alluvial deposits are principally green mudstone and siltstone in the basin depocenter, with fine- to mediumgrained sandstone also present near the eastern basin margin. They are interpreted to have been deposited during intervals of low lake level, during which low-gradient alluvial systems prograded into the basin (Smith et al., 2015). Nine composite alluvial bedsets have been identified and correlated across the basin and named using a letter designation (A-I), starting at the base of the Wilkins Peak Member (Culbertson, 1961).

Lacustrine marlstone in the Wilkins Peak Member is commonly poor in organic carbon but is punctuated by intervals of organic carbon-rich oil shale that are interpreted to reflect the deepening and expansion of Lake Gosiute (Carroll and Bohacs, 2001; Pietras and Carroll, 2006; Smith et al., 2015). Bedded trona (Na₃(CO₃)(HCO₃)•2(H₂O)) and halite are common below the C-bed near the basin depocenter and are typically associated with profundal marlstone (Jagniecki and Lowenstein, 2015). Above the C-bed, evaporite beds are markedly less common and less voluminous, constituting <10% of the estimated commercial trona resources, and their concentration is shifted northward, closer to the geographic center of the Bridger sub-basin (Wiig et al., 1995). Shortite (Na₂Ca₂(CO₃)₃), formed through the diagenetic alteration of gaylussite (Na₂Ca(CO₃)₂)•5(H₂O)) and pirssonite $(Na_2Ca(CO_3)_2) \cdot 2(H_2O)$) at temperatures of >52 °C, is common throughout the Wilkins Peak Member in areas inferred to have experienced burial depths of ~1000 m or more (Jagniecki et al., 2013).

METHODS

Solvay S-34-1 Core

This study evaluates the lowermost 257.29 m of the Solvay S-34-1 core (41.414231°N, 109.69675°W), which is located in the south-central Bridger sub-basin within the basin depocenter (Klonowski et al., 2022). This interval

Figure 3. Generalized stratigraphy of the Solvay S-34-1 core shows the locations of the main radioscopically dated tuffs and time-equivalent surface locations. Within the Wilkins Peak Member, dark gray shading represents alluvial deposits (dominantly green mudstone, green siltstone, and sandstone facies), light gray shading represents bedded evaporite deposits (TB = trona beds), white represents marlstone facies interpreted as underfilled lacustrine deposits, and dashed black lines represent tuffs. U-Pb ages are from Machlus et al. (2015), and the uncertainties shown are analytical uncertainties (2σ). Fm.—formation; Mbr.—member.

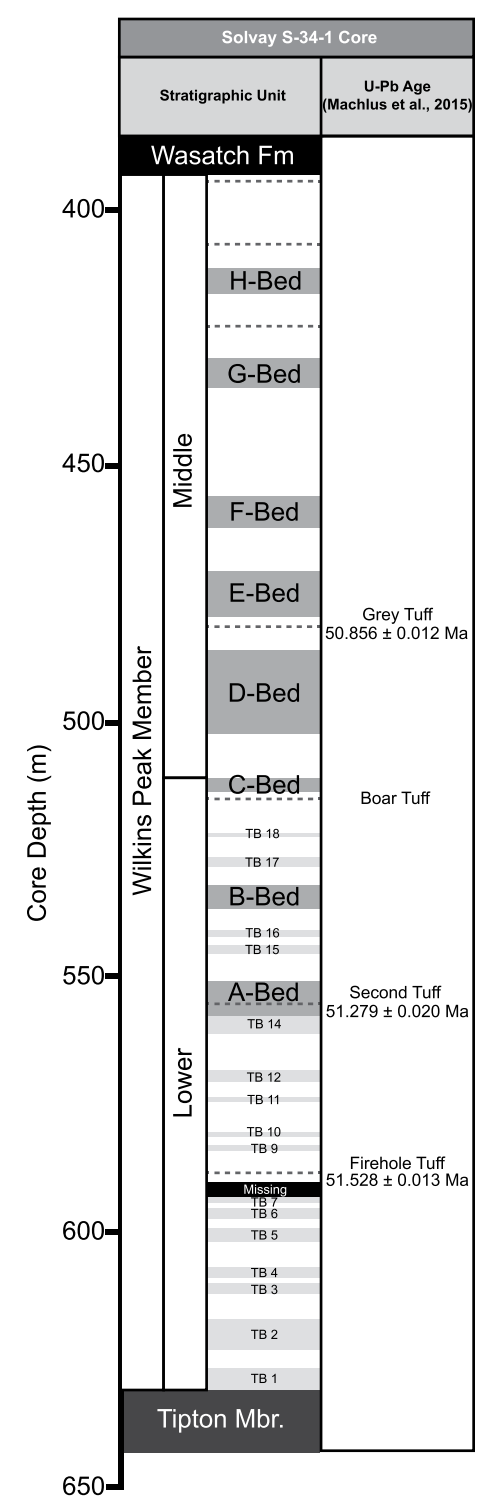
includes 11.78 m of the upper Tipton member, 238.22 m of the overlying lower and middle Wilkins Peak Member, and 7.29 m of deltaic sandstone and oil shale associated with the Desertion Point Tongue of the Wasatch Formation (Sullivan, 1980; Figs. 3 and 4).

Within the Wilkins Peak Member section of this core, dominant lithologies include organic carbon-poor carbonate marlstone, oil shale, green siltstone and mudstone, and bedded evaporite, with minor intervals of volcanic tuff and very fine- to medium-grained sandstone (Klonowski et al., 2022). This interval of core includes 17 bedded evaporite units (TB 1–7 and 9–18) and the A–H-bed sequence of named alluvial beds (Culbertson, 1961; Fig. 3).

XRF Core Scanning

X-ray fluorescence (XRF) core scanning was completed using a third-generation Avaatech XRF core scanner at the University of Wisconsin–Madison, Wisconsin, USA. Prior to scanning, split core samples were placed with the slab face up in the instrument and cleaned of debris, leveled to horizontal, lithologically described, and covered in SPEX 3525 Ultralene foil. For each individual core section, a continuous down-core measurement path was selected to minimize anomalous intervals of core and to avoid cracks, surface irregularities, and localized sedimentary features such as clasts or irregular crystals of evaporite minerals.

XRF core scanning was completed at a continuous 5 mm resolution (5 mm \times 5 mm window size) across the 257.29 m of core. To optimally measure elements Mg-U, two scan runs of each individual core piece were completed using two different sets of instrument settings (10 kV and 30 kV; Table 1). Deconvolution of XRF spectra was completed using a customized deconvolution model in the WinAxil (v. 4.5.2) X-ray analysis software.



We instituted a comprehensive approach to evaluate XRF data quality and reproducibility. To quantify instrument stability during the 14 month analysis period, standards were assessed between each scan of an individual core section (SARM-4; South African Committee for Certified Reference Materials, 1990) and before and after the complete analysis of each

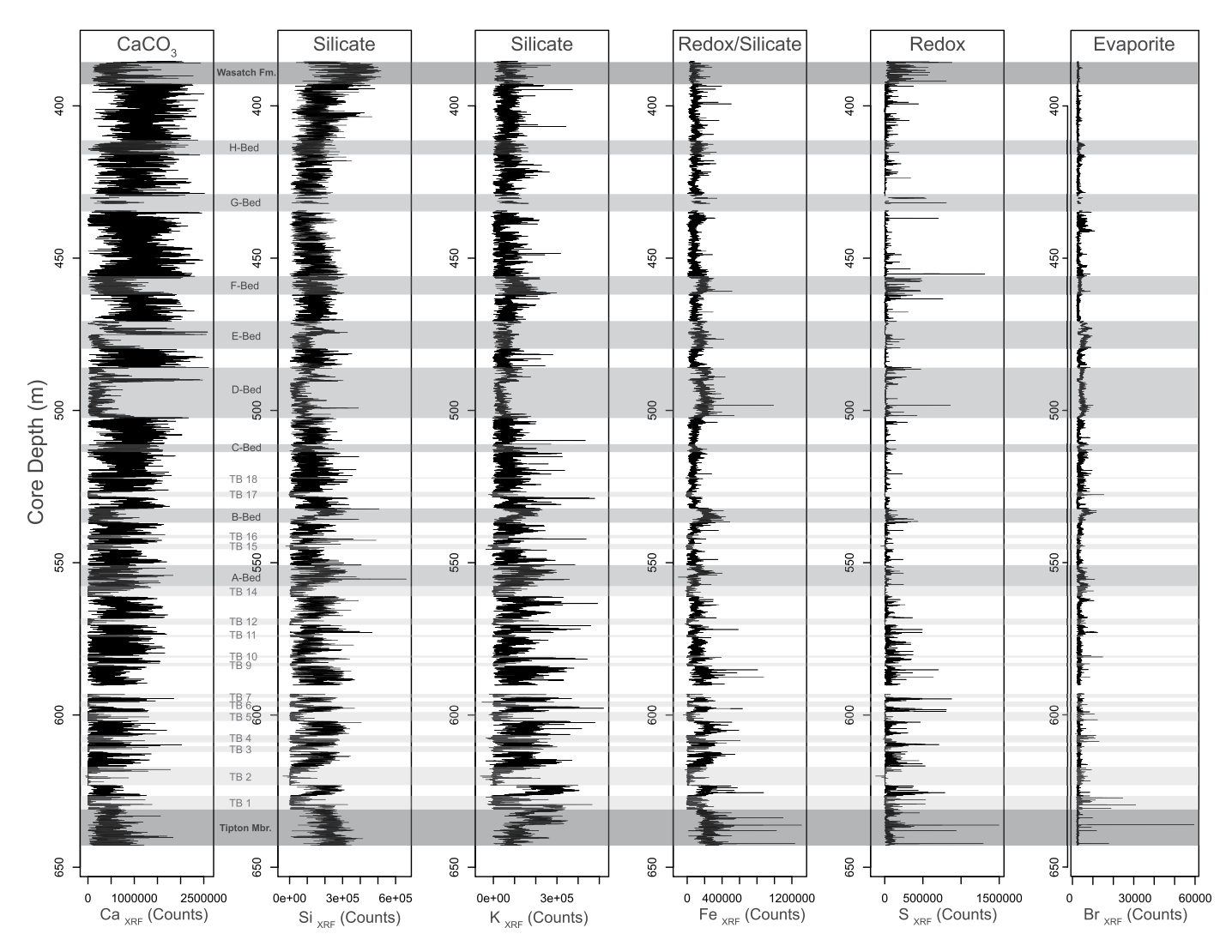


Figure 4. X-ray fluorescence (XRF) core scanner results (in counts) for Ca, Si, K, Fe, S, and Br. Within the Wilkins Peak Member, dark gray shading represents alluvial deposits, light gray shading represents bedded evaporite deposits (TB = trona bed), and white represents lacustrine marlstone deposits. Interpreted mineralogical origin of each element is listed at the top of each record.

individual core section (JGb-1 and JR-1; Imai et al., 1995; Supplemental Material 1¹). To evaluate reproducibility for each element, core sample

¹Supplemental Material. Supplemental Material 1: Measurement of Ca counts in the JR-1 standard, demonstrating the stability of the Avaatech XRF instrument over the 14-month period of study. Supplemental Material 2: Cross plots of 5-mm resolution duplicate measurements of 10 kV and 30 kV elements from scanning of the Solvay S-34-1 core. X- and y-axis units are XRF counts. Supplemental Material 3: Coefficient of variation and the standard deviation of the coefficient of variation results for elements (in counts) at a 5-mm scanning resolution for the Solvay S-34-1 core project. Supplemental Material 4: XRF data (in counts) by depth in the Solvay S-34-1 core for elements Si, S, K, Ca, Fe, and Br. Please visit https://doi.org/10.1130/GSAB.S.21325932 to access the supplemental material, and contact editing@ geosociety.org with any questions.

TABLE 1. X-RAY FLUORESCENCE CORE SCANNER INSTRUMENT SETTINGS USED FOR THE TWO SCAN RUNS OF EACH CORE PIECE

Element	Acceleration voltage	Source current	X-ray filter	Measurement time
Mg to Rh	10 kV	1200 uA	None	20 s
Cu to U	30 kV	1600 uA	Thin Pd	20 s

replicate measurements were taken at every fifth measurement (2.5 cm intervals; Supplemental Material 2; see footnote 1 for all supplemental material). After examination of mean coefficient of variation, standard deviation of the coefficient of variation, and development of cross plots of elemental intensities for all replicate measurements, we identified six key elements (Si, S, K, Ca, Fe, and Br) with superior reproducibility (Supplemental Material 3) from which to analyze the Solvay S-34-1 core.

Over the period of 14 months of XRF scanning, long-term instrumental drift was

observed in the XRF count values for standards (Supplemental Material 1). To account for these artifacts and to minimize the impact of instrumental drift on subsequent data analysis and interpretations, we implemented data corrections on an element-by-element basis using three measured standards (SARM-4, JGb-1, and JR-1). The correction procedure involved the identification and elimination of outlier values in the standard measurements, followed by assessment of long-term drift using a LOW-ESS fit ("noLow" function in the Astrochron package; Meyers, 2014). Details on the drift

TABLE 2. WEIGHTED MEAN U-Pb AGES USED IN THE TUFF CALIBRATION MODEL

Tuff	Age (Ma)	Total uncertainty (Ma)
Grey	50.856	0.060
Second	51.279	0.064
Firehole	51.528	0.061

Note: From Machlus et al. (2015); U-Pb uncertainties are total uncertainties (2σ).

correction procedure are included in Supplemental Material 1.

Chronology Development

Chronologies for the stratigraphic interval were developed using two different approaches. The first approach, designated the tuff calibration (TC) model, uses the published weighted mean U-Pb ages of Machlus et al. (2015) for the Firehole, Second, and Grey tuffs (Table 2) along with the depths of their midpoints in the S-34-1 core (Fig. 3) to calibrate the spatial XRF data to time using piecewise linear interpolation. This approach to building the chronology makes minimal assumptions and uses three control points with low temporal and stratigraphic uncertainty to derive the chronology.

The second method, designated the time-equivalent surface (TES) model, follows the approach of Aswasereelert et al. (2013) to assign ages to 51 time-equivalent surfaces within the Wilkins Peak Member. These time-equivalent

TABLE 3. MODELED AGES FOR THE 30 TIME-EQUIVALENT SURFACES (TESs) IDENTIFIED IN THE S-34-1 CORE

Surface name
Top of H-Bed
10p 0111 200
Top of G-Bed
Top of F-Bed
T (FD)
Top of E-Bed
Grey Tuff
Top of D-Bed
Top of C-Bed
Boar/C-Bed Tuff
Top of B-Bed
·
Top of A-Bed
Second Tuff
Firehole Tuff
Base of Wilkins Peak
Member

Note: These surfaces were calculated using the approach of Aswasereelert et al. (2013) and the weighted mean U-Pb ages of Machlus et al. (2015).

surfaces comprise correlatable tuffs, oil shale beds, and alluvial beds present within the Wilkins Peak Member. The first step in our TES chronology development involves performing a secondorder polynomial fit of the weighted mean U-Pb ages of Machlus et al. (2015; Firehole, Second, Grey, Main, Layered, and Sixth tuffs) to their associated depths within the White Mountain 1 core. This core is located northeast of Solvay S-34-1 (Fig. 1) and was selected because each of the TESs are physically present and unambiguously identifiable at the site, unlike at Solvay S-34-1 (Aswasereelert et al., 2013). Ages for each of the 51 TESs in the White Mountain 1 core are estimated using the polynomial fit, and 30 of the TESs are also identifiable within the Solvay S-34-1 core. The final age model for Solvay S-34-1 is a linear time-depth model using these 30 TESs as control points (Fig. 3; Table 3).

The TES method provides additional timedepth control points over the TC model, which results in more frequent sedimentation-rate adjustments. Through the application of two independent time-depth modeling approaches, we evaluate a range of plausible chronologies rather than relying on one set of sedimentationrate assumptions as the basis of our analysis. This approach also eliminates the need for any astronomical tuning.

Time Series Analysis

Spectral analysis in both depth and time domains was conducted using Astrochron (Meyers, 2014), a software package designed for cyclostratigraphic analysis using the opensource R statistical program (R Core Team, 2021). Multi-taper method (MTM) spectral analysis (Thomson, 1982) was applied to the XRF data set to provide information on oscillatory variability within the data series. This powerspectrum technique, which uses a specified series of prolate tapers for spectral estimation (Thomson, 1982), was applied to the linearly interpolated records of XRF-measured elements using the "mtm" function in Astrochron (Meyers, 2014). Data series were interpolated to their median sampling intervals (0.005 m; Astrochron function "linterp").

To identify cyclic variability and evaluate potential changes in sedimentation rate, evolutive harmonic analysis (EHA)—a method that implements MTM in a moving window—was applied using the "eha" function in Astrochron (Meyers et al., 2001; Meyers, 2014). This analysis is particularly useful for visualizing stratigraphic changes in power, amplitude, and frequency associated with a given cycle of sedimentation. Finally, moving-window cross-correlation was applied to pairs of elements

within the XRF record via the "mwCor" function in Astrochron (Meyers, 2014) to get a more detailed perspective on the interrelationship of element pairs across facies than was possible using a single correlation coefficient for the entire record (Sageman and Hollander, 1999).

RESULTS

Lithofacies Identification and Composition

The XRF elemental record for six key elements (Si, S, Ca, K, Fe, and Br) identifies the main Green River Formation member boundaries and intra-Wilkins Peak Member lithologic variations within the Solvay S-34-1 core (Fig. 4; Supplemental Material 4). Near the base of the core section (631 m depth), the contact between the upper Tipton Member and the lower Wilkins Peak Member is associated with the appearance of bedded evaporite (Fig. 4).

Within the Wilkins Peak Member in the S-34-1 core (392.78-631 m core depth), elemental variations associated with the alternation of lacustrine and alluvial deposits are also observed. Bedded evaporites, one major lithofacies group, range from 0.25 m to 8 m in thickness and are concentrated in the lower Wilkins Peak Member, which is located between the base of the Wilkins Peak Member and the base of the C-bed (Fig. 3). These beds, designated as "TB" (trona beds) in Figures 3 and 4 are associated with an abrupt decrease in elemental counts for most elements. This occurs largely because H, C, O, and Na, the main constituents of trona, are not reliably measurable with an Avaatech XRF core scanner. Br is also present in small amounts, primarily within halite (Higley, 1983), and this element can be reliably evaluated as an indicator element for evaporite deposition (Fig. 4, Supplemental Material 2).

Alluvial beds A-H range from 1.5 m to 16 m thick and are generally associated with elevated Si and K (Figs. 3 and 4), which is consistent with their inferred terrigenous silicate origin. Within alluvial beds, consistently low counts were measured for Ca, an indicator element for calcium carbonate content (Fig. 4). Counts of Fe are elevated in alluvial beds, and this is likely the result of more abundant detrital iron oxide input or diagenetic formation of iron oxides in situ in an oxic environment (Fig. 4). Additionally, increased Fe counts also appear to reflect redox conditions in the Wilkins Peak Member as a result of its inclusion in pyrite, pyrrhotite, marcasite, and other diagenetic sulfide minerals (Bradley and Eugster, 1969; Sheriff and Shive, 1982; Klonowski et al., 2022).

Marlstone, the dominant lacustrine lithofacies of the middle Wilkins Peak Member in the

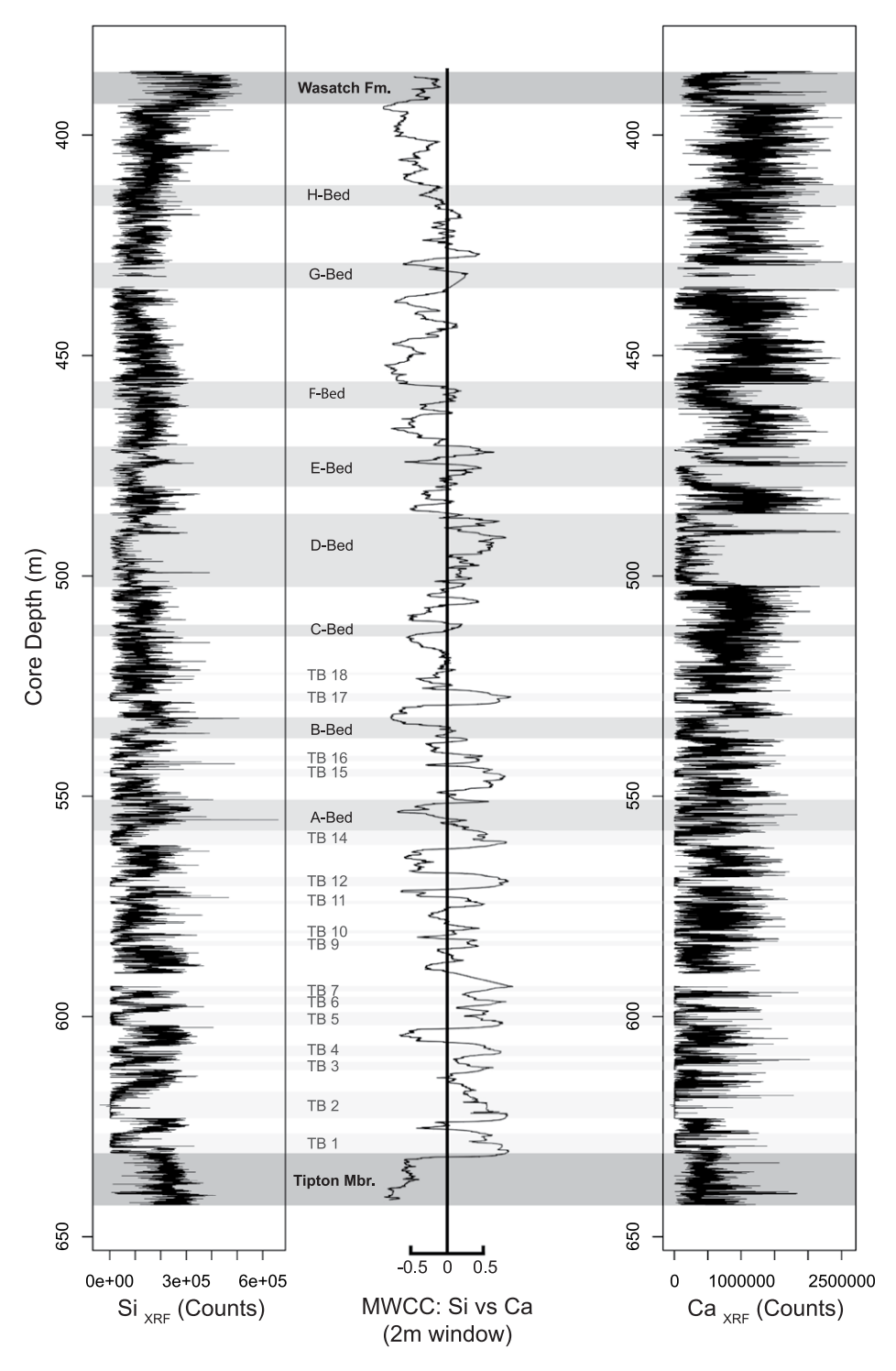


Figure 5. Moving window cross correlation (MWCC) of the Ca and Si X-ray fluorescence (XRF) data is shown. The MWCC correlation coefficient is represented by the center panel. Within the Wilkins Peak Member, dark gray shading represents alluvial deposits, light gray shading represents bedded evaporite deposits ($TB = trona\ bed$), and white represents lacustrine marlstone deposits. Fm.—formation; Mbr.—member.

S-34-1 core, is characterized by high, but variable, counts in calcium carbonate indicator elements, including Ca, and siliciclastic indicator elements, including Si and K (Fig. 4). Previous

mineralogic assessments of Green River Formation marl and oil shale found that they commonly contain calcite, dolomite, quartz, alkali feldspar, plagioclase, and illite and other clay minerals (Bradley and Eugster, 1969; Hosterman and Dyni, 1972; Picard and High, 1972; Robb and Smith, 1974; Dyni, 1976; Mason, 1987). This mineral assemblage is consistent with our XRF results for these facies. Moving-window cross-correlation analysis of Si and Ca shows a largely negative Pearson correlation coefficient in the marlstone facies, which suggests a generally antithetic relationship between calcium carbonate and silicate inputs (Fig. 5).

Similar alternations of inferred calcium carbonate and siliciclastic lithologies have been observed in carbonate marl and oil shale in other basins of the Green River Formation, such as the Parachute Creek Member of the Uinta Basin of Utah (Walters et al., 2020). S counts are variable across the Wilkins Peak Member, particularly in the carbonate marlstone of the lower Wilkins Peak Member. Sulfate-bearing minerals are not observed in the Wilkins Peak Member, likely due to sulfate-reduction in the surface sedimentary environments (Bradley and Eugster, 1969). Instead, this S is in the form of either elemental sulfur in organic matter or, when paired with corresponding increases in Fe counts, diagenetic sulfide minerals such as pyrite, pyrrhotite, and marcasite (Bradley and Eugster, 1969; Sheriff and Shive, 1982; Klonowski et al., 2022). Sulfide minerals and elemental sulfur preserved in organic matter have been interpreted to record low-oxygen conditions in other modern lakes and paleolakes (Demaison and Moore, 1980; Johnson, 1981; Kelts, 1988; Tänavsuu-Milkeviciene and Sarg, 2012).

Above the H-bed of the Solvay core and near the top of the study section, we observe a major depositional shift from the lacustrine and alluvial deposits of the Wilkins Peak Member to oil shale and fine- to medium-grained, massive- to crossbedded sandstone (Klonowski et al., 2022). We attribute these 8.29 m of fluvial-lacustrine deposits to the Desertion Point Tongue of the Wasatch Formation (Sullivan, 1980). Moving into this sandstone- and oil shale-dominated interval, calcium carbonate indicator element (Ca) counts decrease, while siliciclastic (Si and K) and select redox (S) indicator element counts increase (Fig. 4).

Spectral Analysis in the Time Domain

The TC and TES chronologies demonstrate broadly consistent net accumulation rates (Fig. 6). The TC method models net accumulation rates ranging from 132 μ m/yr to 174 μ m/yr for the lower and middle Wilkins Peak Member (median: 153 μ m/yr; Fig. 6). The time-equivalent surface method, which utilizes 27 additional time-control points, generates net accumulation rates on the order of 38–1300 μ m/yr (median:

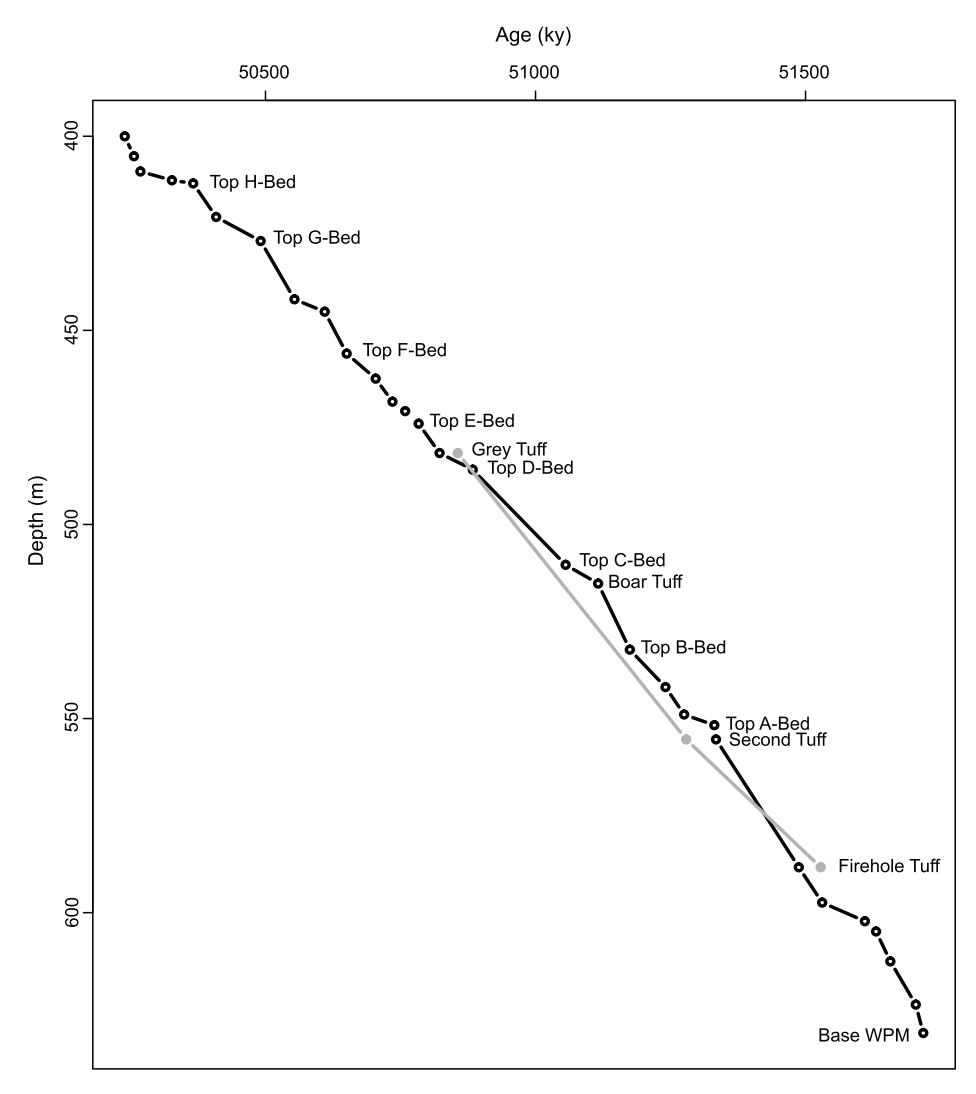


Figure 6. Time-depth control points used in the temporal calibration of the X-ray fluorescence data are plotted, with the tuff calibration model (TC) in gray with filled depth-time control points, and time-equivalent surface (TES) model in black with open depth-time control points. WPM—Wilkins Peak Member.

 $160.5 \,\mu\text{m/yr}$) for the lower and middle Wilkins Peak Member. The highest net accumulation rates in the TES model are observed within the A-bed, the only interval of this core in which there are two TES surfaces located within an alluvial bed (Fig. 6). Although bedded evaporite facies are too finely bedded to be discretely resolved in the TES model, modern examples, such as the halite deposits of the Dead Sea, suggest that depositional rates were far higher than that of other facies preserved in the Wilkins Peak Member (Lensky et al., 2005; Kiro et al., 2016; Lowenstein et al., 2021).

Within the EHA plots for the TC- and TES-calibrated Si, K, Ca, Fe, and Br records, a clear transition in the frequency distribution of power and amplitude is present near the top of the C-bed at ca. 51 Ma (Figs. 7 and 8). Below this 51 Ma

transition, in the lower Wilkins Peak Member, where bedded evaporites are present, Si and K show strong, stratigraphically continuous peaks in power and amplitude across a broad range of frequencies in both chronologies (Fig. 7). Above this 51 Ma transition, where bedded evaporites are not present in the Solvay S-34-1 core, the strongest power and amplitude in Si and K is concentrated predominantly in lower frequencies (<0.011 cycle/k.v.; period: >90 k.v.) in both chronologies (Fig. 7). EHA results for Ca show strong, stratigraphically continuous amplitudes in the low frequencies for the interval younger than 51 Ma, a response opposite of Si and K (Fig. 8). This strong middle Wilkins Peak Member response in Ca corresponds with the alternating deposition of lacustrine carbonate marls and alluvial siliciclastic mudstone,

siltstone, and sandstone present in the middle Wilkins Peak Member (Fig. 8). Additionally, within the EHA plots for Si, K, Ca, Fe, and Br, amplitude and frequency modulation of the presumed short eccentricity signal has an ~400 k.y. (long eccentricity) recurrence, as predicted by astronomical theory; this is particularly well expressed in TES-calibrated Ca and Fe (see white arrows in Figs. 7 and 8).

Based on the EHA results, the XRF data set can be divided into the lower Wilkins Peak Member and middle Wilkins Peak Member intervals across the observed ca. 51 Ma power and amplitude transition (Figs. 7 and 8). As expected, the power spectral results for these two intervals are markedly different (Fig. 9). Within the TC- and TES-calibrated records for the middle Wilkins Peak Member, variance in Si, S, K, Ca, and Fe is generally concentrated at frequencies less than 0.015 cycle/k.y. (period: >67 k.y.; Fig. 9). In this low-frequency range, Si, S, Ca, K, Fe, and Br records for the middle Wilkins Peak Member show a strong power peak between 0.0 and 0.004 cycle/k.y. (period: >250 k.y.), and K, Ca, Fe, and Br show a prominent 0.01 cycle/k.y. (period: 100 k.y.) power peak (Fig. 9). Within the Si, S, Ca, K, Fe, and Br spectral results for the middle Wilkins Peak Member, power peaks at frequencies greater than 0.01 cycle/k.y. (period: <100 k.y.) are muted compared to the low frequencies (Fig. 9).

Within the TC- and TES-calibrated records for the lower Wilkins Peak Member, the largest peaks in power for Si, S, K, Ca, Fe, and Br are shifted to higher frequencies relative to the largest peaks in power for the middle Wilkins Peak Member (Fig. 9). In power spectra for lower Wilkins Peak Member Si, S, K, and Fe, these peaks are higher in magnitude than those observed at corresponding frequencies in the middle Wilkins Peak Member spectra (Fig. 9). Only the upper Wilkins Peak Member Ca and Br records show sub-eccentricity power peaks of similar magnitude to those of the lower Wilkins Peak Member records for these two elements (Fig. 9). MTM spectra of Si, S, and K in the lower Wilkins Peak Member show little power concentrated at frequencies lower than 0.007 cycle/k.y. (period: 143 k.y.), unlike what is observed in the middle Wilkins Peak Member (Fig. 9). Within these lower Wilkins Peak Member Si and K records, the major peaks in power are observed around 0.010-0.020 cycle/k.y. (period: 50-100 k.y.), 0.025 cycle/ k.y. (period: 40 k.y.), 0.039-0.043 cycle/k.y. (period: 23-25 k.y.), and 0.052 cycle/k.y. (period: 19.2 k.y.; Fig. 9). MTM spectra of S, Ca, and Br from the lower Wilkins Peak Member show power peaks at \sim 0.020–0.025 cycle/k.y. (period: 40-50 k.y.), 0.035-0.043 cycle/k.y. (period: 23-28 k.y.), and 0.051

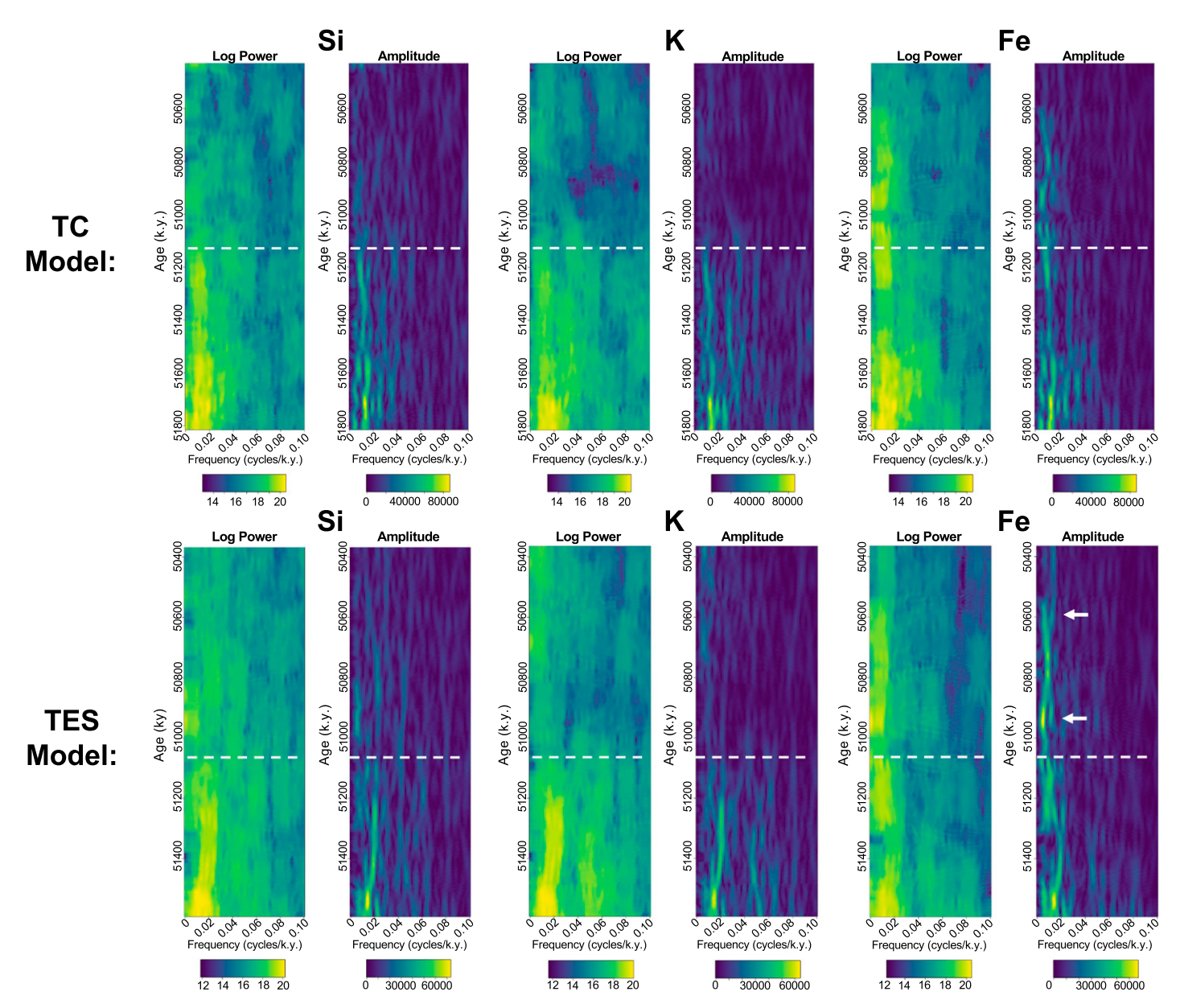


Figure 7. Evolutive harmonic analysis (EHA; $3-2\pi$ discrete prolate spheroidal sequence [DPSS] tapers, 250 k.y. window) plots are shown for drift-corrected Si, K, and Fe elemental records temporally calibrated using the tuff calibration (TC) method in the upper panel and time-equivalent surface (TES) method in the lower panel. Each 250 k.y. window was linearly detrended prior to analysis. The horizontal white dotted line within the EHA plots shows the location of the top of the C-bed, and the white arrows in Fe highlight amplitude and frequency modulation of the presumed short eccentricity signal by the ~400-k.y.-long eccentricity cycle.

cycle/k.y. (period: 19.6 k.y.), but also display additional strong low-frequency (<0.01 cycle/k.y.; > 100 k.y.) and high-frequency (>0.06 cycle/k.y.; <16.7 k.y.) variability (Fig. 9). MTM spectra for Fe from the lower Wilkins Peak Member show a broad peak in power from 0.0025 cycle/k.y. to 0.025 cycle/k.y. (period: 40–400 k.y.) centered around 0.01 cycle/k.y. (period: 100 k.y.), with additional minor peaks in power between 0.04 and 0.07 cycle/k.y. (period: 14–25 k.y.; Fig. 9).

DISCUSSION

Identification of a Mid-Wilkins Peak Member Transfer Function Transition

Due to its resolution, continuity, and the wide range of elements measured, XRF data provide an opportunity for a cyclostratigraphic characterization of the Wilkins Peak Member at a breadth and level of detail not previously achievable. Broadly, these results are consistent

with previous cyclostratigraphic assessments of the Wilkins Peak Member, which have identified eccentricity, obliquity, precession, and sub-precession—scale variability (Pietras et al., 2003a; Meyers, 2008; Machlus et al., 2008; Aswasereelert et al., 2013). However, analysis of these new data also reveals a distinct shift in the frequency distribution of power and amplitude between the lower and middle Wilkins Peak Member, which coincides with the end of bedded evaporite deposition in the Solvay S-34-1 core.

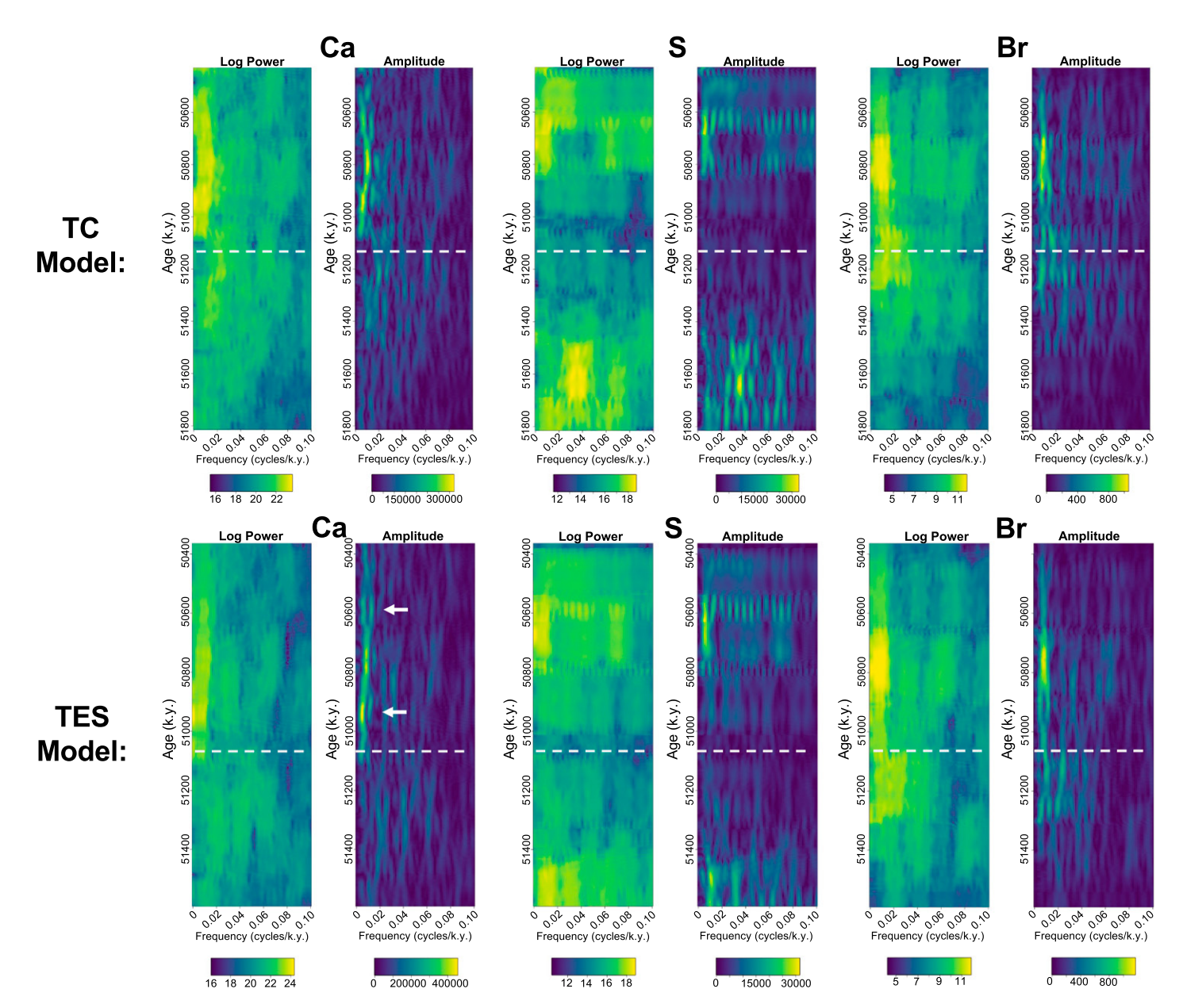


Figure 8. Evolutive harmonic analysis (EHA; $3-2\pi$ discrete prolate spheroidal sequence [DPSS] tapers, 250 k.y. window) plots are shown for drift-corrected Ca, S, and Br elemental records temporally calibrated using the tuff calibration (TC) method in the upper panel and time-equivalent surface (TES) method in the lower panel. Each 250 k.y. window was linearly detrended prior to analysis. The horizontal white dotted line within the EHA plots shows the location of the top of the C-bed, and the white arrows in Ca highlight amplitude and frequency modulation of the presumed short eccentricity signal by the ~400-k.y.-long eccentricity cycle.

In the lower Wilkins Peak Member, MTM spectra and EHA plots of temporally calibrated Si, S, K, Ca, Fe, and Br show strong peaks in power and amplitude across a range of frequencies, particularly in the frequency bands associated with short eccentricity, obliquity, and precession, and sub-precession cycles (Figs. 7–9). Identification of short eccentricity-scale variability in our lower Wilkins Peak Member record is consistent with the findings of previous Wilkins Peak Member studies,

which have identified short eccentricity pacing of alternations in alluvial and lacustrine deposition across the Wilkins Peak Member (Aswasereelert et al., 2013; Smith et al., 2014b). This basin-scale oscillation between lacustrine and alluvial depositional modes, which starts in the lower Wilkins Peak Member and continues throughout the middle Wilkins Peak Member, is thought to result from eccentricity-scale influences on precipitation and evaporation processes around Lake Gosiute,

which impacted both lake depth and extent as well as regional rates of sedimentary advection (Smith et al., 2014b). During the alluvial mode of deposition in Lake Gosiute, low water levels in the Bridger sub-basin permitted low-gradient alluvial systems to prograde into the basin, depositing siliciclastic sediments rich in Si, K, and Fe, but poor in Ca. During the lacustrine mode of deposition, higher water levels enhanced production of Ca-rich lacustrine calcium carbonates, which mixed with

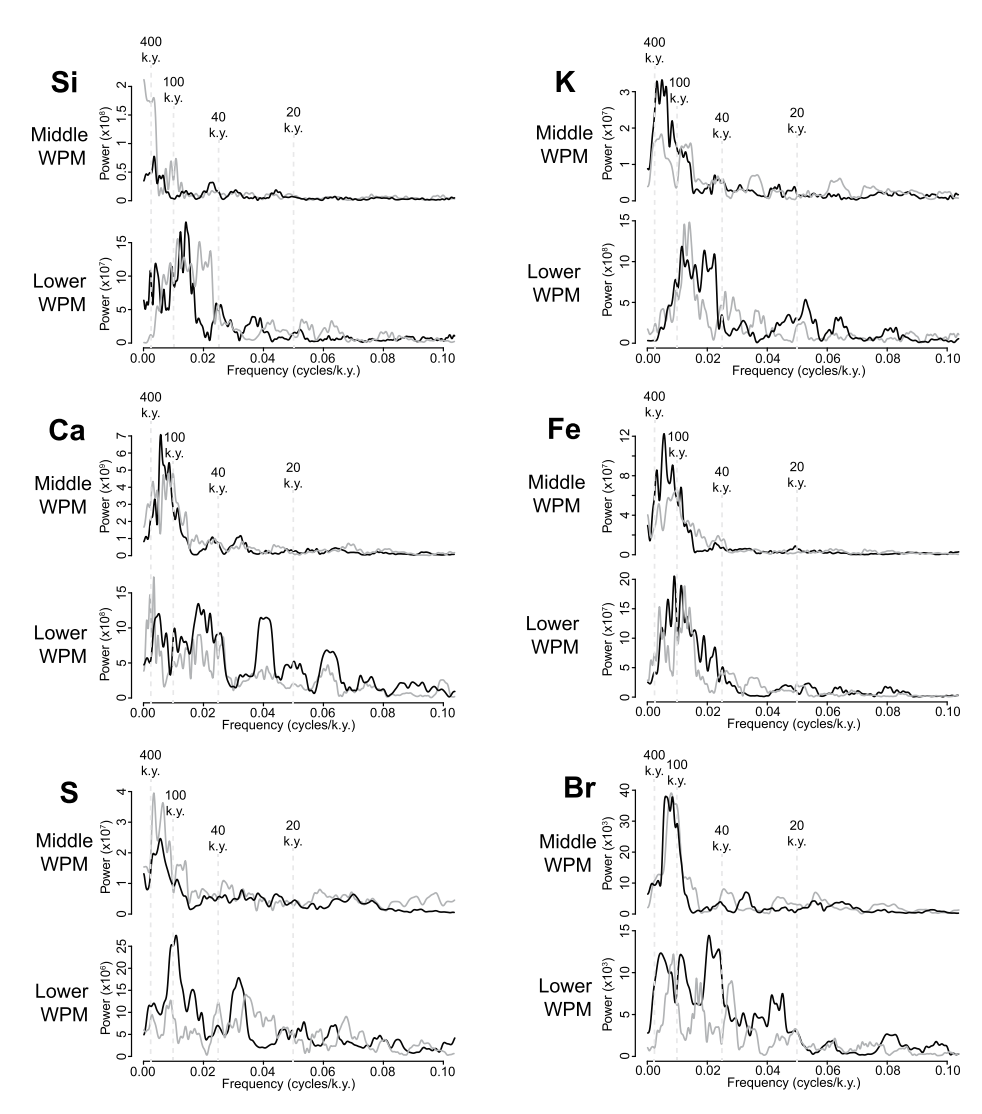


Figure 9. Multi-taper method (MTM) power spectra (3–2 π discrete prolate spheroidal sequence [DPSS] tapers) are shown for drift-corrected, linearly detrended, temporally calibrated Si, K, Ca, Fe, S, and Br elemental records for the middle Wilkins Peak Member (WPM) and lower Wilkins Peak Member intervals. Tuff calibration (TC) model results are in gray, and time-equivalent surface (TES) model results are in black. Dashed light gray lines denote periods of 400 k.y., 100 k.y., 40 k.y., and 20 k.y.

siliciclastic input into the lake to produce lacustrine marlstones.

Strong sub-eccentricity-scale variability also present in the lower Wilkins Peak Member appears to reflect changes in the depth of Lake Gosiute during its deposition in response to precession and obliquity influence on water input and evaporation in the basin (Aswaser-eelert et al., 2013; Smith et al., 2014b). During highstands, the lake's increased depth enabled stratification, enhancing the preservation of Br-rich evaporite deposits and S-rich organic material and sulfides in the basin center. During lowstands, the basin center saw enhanced input of Si- and K-rich siliciclastic sediments,

although these shallower conditions were less favorable to the preservation of evaporite, organic material, and sulfides due to more enhanced mixing of the lake. Our lower Wilkins Peak Member spectral results also show peaks in power at sub-precessional periodicities (<18 k.y.), a temporal scale that is consistent with a range of interpreted lake expansion cycles of \sim 10 k.y. average duration identified by Pietras et al. (2003a).

In contrast to the lower Wilkins Peak Member, MTM spectra and EHA plots of temporally calibrated Si, K, Ca, Fe, and Br from the middle Wilkins Peak Member show dominant low-frequency forcing in the frequencies asso-

ciated with long and short eccentricity, with less power concentrated in the frequencies associated with obliquity, precession, and subprecession cycles (Figs. 7–9). This shift to the lower frequencies in power spectra from the middle Wilkins Peak Member is coincident with the reduction in bedded evaporites in the Solvay S-34-1 core, leaving the continued eccentricity-paced alternations in alluvial siliciclastic and lacustrine calcium carbonate deposition as the largest shifts in lithology across the middle Wilkins Peak Member. The strong influence of this cyclic alternation in depositional mode on the sedimentary record of the middle Wilkins Peak Member, in combination with reduced lithologic contrast following the disappearance of the bedded evaporites in the Solvay S-34-1 core, appear to have contributed to a more prominent low-frequency signal in the middle Wilkins Peak Member relative to the lower Wilkins Peak Member. Although dominated by low-frequency forcing, the middle Wilkins Peak Member does show evidence of minor sub-eccentricity scale cyclic variability in Si, S, K, Ca, Fe, and Br (Fig. 9), which likely reflects variations in siliciclastic input resulting from changing fluvial input to the lake or avulsion of the alluvial plain as well as variations in the preservation of organic S, sulfide minerals, and evaporite as a result of stratification during lake highstands.

Overall, this analysis suggests that the lower Wilkins Peak Member was more sensitive to higher-frequency obliquity, precession, and sub-Milankovitch-scale variability than the middle Wilkins Peak Member. Given the sedimentation-rate corrections made in each of the two chronologies, based on high-precision radioisotopic ages from tuffs found at known depths in the S-34-1 core, we do not anticipate that uncorrected sedimentation-rate changes are generating such a major stratigraphic shift in the frequency distribution of power and amplitude between the lower and middle sections of the Wilkins Peak Member. Astrochronologic analyses of coeval deep marine records do not suggest any abrupt changes in astronomical forcing around 51 Ma (Westerhold and Röhl, 2009; Westerhold et al., 2018). Instead, we posit that this mid-Wilkins Peak Member shift in variance distribution is predominantly an expression of a change in the depositional transfer function within the Wilkins Peak Member rock record. In this case, an environmental shift in the Lake Gosiute system around the deposition of the C-bed led to a marked reduction of bedded evaporite deposition, a facies that appears to be associated with a greater sensitivity to obliquity, precession, and sub-Milankovitch-scale cyclicity.

Mechanisms for Changing the Wilkins Peak Member Transfer Function

We hypothesize that the observed shift in the expression of Milankovitch-band cyclicity—the depositional transfer function—could result from an environmental change in the lake that acted to disrupt the formation or preservation of bedded evaporites above the mid-Wilkins Peak Member transition. Studies of modern bedded evaporite deposits, such as those of the Dead Sea, suggest that deep, stratified, hypersaline, perennial lakes are highly conducive to bedded evaporite precipitation and preservation especially below wave base and a thermocline (Kiro et al., 2016; Sirota et al., 2016, 2017; Demicco and Lowenstein, 2020). This is largely because evaporite minerals are highly sensitive to temperature and salinity changes, and to mixing processes, which can act to dissolve bedded evaporite deposited in shallower environments. The close association of bedded trona and halite with organic carbonrich oil shale facies in the S-34-1 core supports a stratified lake as an environmental key for the deposition and preservation of these bedded evaporite facies in the Wilkins Peak Member.

A mid-Wilkins Peak Member shift in the climate system during the EECO greenhouse climate could have resulted in changes to the hydrologic balance of the lake basin, the temperature of the lake, and the intensity of evaporative processes, each of which would have impacted evaporite deposition and preservation. For example, a climate-driven increase in water input into the lake basin could act to freshen the lake, weaken the lake's chemocline, and induce lake mixing, all of which would be unfavorable to the formation and preservation of bedded evaporites. Alternatively, a tectonically driven mid-Wilkins Peak Member change in lake-basin morphology could alter the depth and extent of the lake in a way that would be unfavorable for evaporite preservation.

Carbonate $\delta^{18}O$ from samples spanning the Wilkins Peak Member shows no systematic change from the lower Wilkins Peak Member to the middle Wilkins Peak Member (R.D. Norris, 2018, personal commun.). These results provide no conclusive evidence for climate-driven enhancement of evaporation or precipitation processes. 87Sr/86Sr ratios (Doebbert et al., 2014) also show minimal variation across the Wilkins Peak Member, which suggests there were no fundamental changes in hydrologic sourcing during deposition of the Wilkins Peak Member. Furthermore, aside from the reduction in bedded evaporite deposition in the basin depocenter, Wilkins Peak Member lithofacies show no major longterm shifts across the proposed transfer-function transition (Smith et al., 2015; Klonowski et al.,

2022). Alternations between lacustrine carbonate and alluvial siliciclastic deposits start in the lower Wilkins Peak Member and continue similarly in the middle and upper Wilkins Peak Member even after the disappearance of bedded evaporites in the S-34-1 core (Fig. 4). While not present above the lower Wilkins Peak Member in the S-34-1 core, bedded evaporite is observed to a more limited extent in the middle and upper Wilkins Peak Member in more northerly locations in the Bridger sub-basin (Fig. 2; Dyni, 1997). Additionally, the presence of shortite and northupite in the middle Wilkins Peak Member of the Solvay S-34-1 core also suggests continued arid conditions above the proposed transferfunction transition, since groundwater brines are necessary for their formation during early diagenesis and prior to compaction (Jagniecki et al., 2013; Olson and Lowenstein, 2021; Klonowski et al., 2022).

Moreover, bedded evaporite units younger than the mid-Wilkins Peak Member transition are found in Green River Formation deposits in neighboring basins. Bedded halite and nahcolite in the Piceance Basin was deposited in the Parachute Creek Member subsequent to deposition of the Skyline Tuff, which has an 40Ar/39Ar age of 49.58 ± 0.28 Ma (Dyni, 1974; Smith and Carroll, 2015; Tänavsuu-Milkeviciene et al., 2017; Birgenheier et al., 2020). This timing approximately coincides with deposition of the lower Laney Member in the Bridger sub-basin, which lacks bedded evaporite. Bedded halite and trona in the Uinta Basin are younger still, postdating the Fat Tuff, which has an 40Ar/39Ar age of 46.62 ± 0.13 (Dyni et al., 1995; Smith et al., 2008, 2010; Vanden Berg and Birgenheier, 2017). The diachroneity of bedded evaporite preserved in several adjacent basins clearly demonstrates that climate alone cannot explain its origin and that individual basin evolution plays a significant role.

Given the lack of evidence for an abrupt change in the mean climate state, we propose that structural changes occurring along

the northern Uinta Mountain Uplift were the dominant influence on this mid-Wilkins Peak Member transfer-function transition. Northward Laramide thrusting along the Uinta-Sparks fault system north of the Uinta Mountains was accompanied by downward flexure of the adjacent southern edge of the greater Green River Basin, which resulted in southward thickening of Green River Formation deposits (Sears et al., 1982; Hansen, 1986; Roehler, 1992). Based on mapping by Roehler (1993), this fault system intersects the lower Wilkins Peak Member and terminates in the Cathedral Bluffs member, with the overlying Laney Member remaining undisturbed by the fault. This relationship is broadly consistent with Wilkins Peak Member thickness patterns that evolve from an asymmetric southern depocenter in the lower to middle Wilkins Peak Member, to more uniform thickness across the Bridger sub-basin in the upper Wilkins Peak Member (Roehler, 1992; Smith et al., 2015). We therefore conclude that active movement on the Uinta-Sparks fault system ceased during deposition of the middle Wilkins Peak Member, which resulted in decreased rates of accommodation in the southern Bridger sub-basin.

We propose that this tectonically induced change in lake-basin morphology altered the mode of evaporite deposition within Lake Gosiute during deposition of the Wilkins Peak Member and was thus responsible for the observed change in the rhythm of bedded evaporite deposition in the paleolake (Fig. 10). During deposition of the lower Wilkins Peak Member—prior to the deposition of the C-bed-the continued active movement of the Uinta-Sparks thrust system provided accommodation in the south-central Bridger sub-basin, near the location of the S-34-1 core (Fig. 1). This allowed a narrow, deep, perennial, meromictic lake to form around the depocenter during deposition of much of the lower Wilkins Peak Member (Fig. 10). Due to the lake's depth at astronomically paced highstands, a thermocline and chemocline could

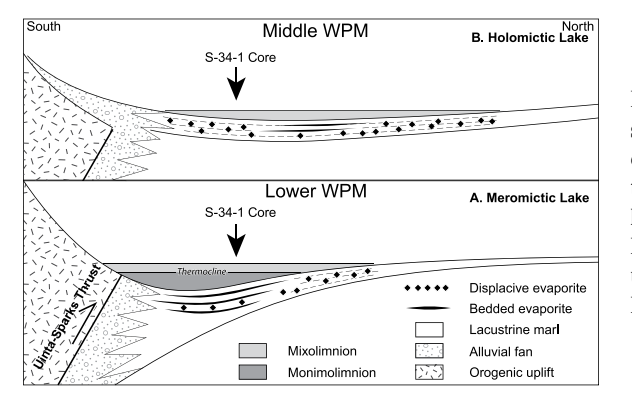


Figure 10. Schematic model is shown for a tectonically driven change in the depositional transfer function between (A, lower panel) the lower Wilkins Peak Member (WPM) and (B, upper panel) middle Wilkins Peak Member.

be maintained, permitting bedded evaporite formation and preservation below wave base due to the denser, colder, more saline monimolimnion of the lake (Fig. 10). Outside of the basin depocenter and above the level of the lake's thermocline and chemocline, bedded evaporites were not preserved due to seasonal changes in lake temperature and evaporation rates that produced yearly cycles of precipitation followed by dissolution.

With the cessation of movement on the Uinta-Sparks fault system, accommodation rates in the south-central Bridger sub-basin waned, and the depocenter began to infill and shift northward, also moving the locus of bedded evaporite deposition northward and away from the location of the S-34-1 core (Fig. 10). This shift produced a broader, shallower, more expansive Lake Gosiute during deposition of the middle Wilkins Peak Member. The additional surface area and reduced water depth likely led to more prevalent holomictic lake conditions due to enhanced wind-driven mixing, preventing the formation of a sustained thermocline or chemocline. Seasonal warming of lake waters likely led to enhanced evaporite dissolution, as occurs in the shallow margins of the Dead Sea today (Sirota et al., 2016, 2017). The shallower lake also allowed more frequent exposure of the lake floor, which exposed any primary bedded evaporite to freshwater dissolution. This enhanced dissolution contributed to the omission of bedded evaporite from the rock record of the middle Wilkins Peak Member in the S-34-1 core, with middle and upper Wilkins Peak Member bedded evaporites only found in limited zones within the northernshifted depocenter, where conditions were most favorable for preservation. Instead, evaporites were deposited as early diagenetic displacive crystals in the southern Bridger sub-basin at the location of the S-34-1 core, which were less susceptible to dissolution by the warm waters of the lake than bedded evaporites but failed to record a similar signature of cyclic variability. Initially composed of gaylussite or pirssonite that was later diagenetically altered to shortite, these displacive evaporites grew within the sediment under specific brine chemistry and temperatures. Stability in these conditions was required for these minerals to be preserved in the rock record (Jagniecki et al., 2013).

CONCLUSIONS

The application of XRF core scanning to the Wilkins Peak Member of the Green River Formation provides one of the most detailed multielement assessments of an ancient lake system, with the goal of characterizing cyclic sedimentation within the Wilkins Peak Member of the Green River Formation at a previously unattainable level of detail, assessing changes in the expression of cyclic sedimentation, and evaluating potential depositional transfer-function linkages to changes in climate, tectonics, and landscape evolution.

Overall, our analysis of key XRF paleoenvironmental indicator elements in the S-34-1 core shows consistency with previous cyclostratigraphic assessments of the Wilkins Peak Member, indicating eccentricity, obliquity, precession, and sub-precession–scale cyclicity. More importantly, however, our analysis of this XRF data set highlights a previously unrecognized shift in the frequency distribution of variance between the lower Wilkins Peak Member and the middle Wilkins Peak Member, which coincides with the decline of bedded evaporite deposition at ca. 51 Ma.

We attribute this shift to a change in the transfer function, which encodes environmental signals into the preserved Wilkins Peak Member rock record. Given that available geochemical, sedimentological, and stratigraphic evidence appears to rule out a climatic trigger for this change in the transfer function, we propose that a structural change to the Bridger sub-basin resulting from the mid-Wilkins Peak Member deactivation of a Uinta Mountain thrust fault caused Lake Gosiute to transform from a deep, meromictic lake that was able to deposit bedded evaporites in its depocenter to a shallow, broad, holomictic lake with temperatures and salinities too variable to permit the preservation of bedded evaporites. As a result, the transfer function of the lower Wilkins Peak Member could encrypt environmental signals present in bedded evaporite deposits, while the transfer function of the middle Wilkins Peak Member could not. These results underscore the need for careful integration of basin and depositional system history with cyclostratigraphic interpretation of the dominant astronomical signals preserved in the stratigraphic archive.

ACKNOWLEDGMENTS

We thank M. Paperini and Solvay Chemicals, Inc., for the use of the Solvay S-34-1 core. E. Klonowski, S. Honig, I. Sageman, and M.E. Smith assisted with the preparation, imaging, and logging of the core. We also thank A. Cohen for his thorough and insightful comments, which improved this manuscript, and M.E. Smith for his helpful feedback over the course of this project. This study received financial support from the National Science Foundation Integrated Earth Systems Program (NSF-EAR 1813278 and 1812741), the National Science Foundation Early Career Development Program (NSF-EAR 1151438), the Geological Society of America Graduate Research Grant Program, the American Association of Petroleum Geologists Foundation Grants-in-Aid program, and the Department of Geoscience at the University of Wisconsin-Madison.

REFERENCES CITED

- Aswasereelert, W., Meyers, S.R., Carroll, A.R., Peters, S.E., Smith, M.E., and Feigl, K.L., 2013, Basin-scale cyclostratigraphy of the Green River Formation, Wyoming: Geological Society of America Bulletin, v. 125, p. 216–228, https://doi.org/10.1130/B30541.1.
- Bernhart Owen, R., Renaut, R.W., Muiruri, V.M., Rabideaux, N., Lowenstein, T.K., McNulty, E.P., Leet, K., Deocampo, D., Luo, S., Deino, A.L., Cohen, A., Sier, M.J., Dupont-Nivet, G., Campisano, C., Shen, C.C., Billingsley, A., Mbuthia, A., and Stockhecke, M., 2019, Quaternary history of the Lake Magadi Basin, southern Kenya Rift: Tectonic and climatic controls: Palaeogeography, Palaeoclimatology, Palaeoecology, v. 518, p. 97–118, https://doi.org/10.1016/j.palaeo.2019.01.017.
- Birgenheier, L.P., Berg, M.D.V., Plink-Björklund, P., Gall, R.D., Rosencrans, E., Rosenberg, M.J., Toms, L.C., and Morris, J., 2020, Climate impact on fluvial-lake system evolution, Eocene Green River Formation, Uinta Basin, Utah, USA: Geological Society of America Bulletin, v. 132, no. 3–4, p. 562–587, https://doi.org/10.1130 /B31808.1.
- Bradley, W.H., 1929, The varves and climate of the Green River epoch: U.S. Geological Survey Professional Paper 158-E, p. 87–110.
- Bradley, W.H., and Eugster, H.P., 1969, Geochemistry and paleolimnology of the trona deposits and associated authigenic minerals of the Green River Formation of Wyoming: U.S. Geological Survey Professional Paper 496-B, https://doi.org/10.3133/pp496B.
- Carroll, A.R., and Bohaes, K.M., 1999, Stratigraphic classification of ancient lakes: Balancing tectonic and climatic controls: Geology, v. 27, p. 99–102, https://doi.org/10.1130/0091-7613(1999)027<0099:SCOALB>2 3.CO:2.
- Carroll, A.R., and Bohacs, K.M., 2001, Lake-type controls on petroleum source rock potential in nonmarine basins: AAPG Bulletin, v. 85, p. 1033–1053.
- Carroll, A.R., Graham, S.A., and Smith, M.E., 2010, Walled sedimentary basins of China: Basin Research, v. 22, p. 17–32, https://doi.org/10.1111/j.1365-2117.2009 .00458.x.
- Cohen, A.S., 2003, Paleolimnology: The History and Evolution of Lake Systems: New York, Oxford, Oxford University Press, 500 p., https://doi.org/10.1093/oso/9780195133530.001.0001.
- Cohen, A.S., et al., 2007, Ecological consequences of early late Pleistocene megadroughts in tropical Africa: Proceedings of the National Academy of Sciences of the United States of America, v. 104, p. 16,422–16,427, https://doi.org/10.1073/pnas.0703873104.
- Culbertson, W.C., 1961, Stratigraphy of the Wilkins Peak member of the Green River Formation, Firehole Basin Quadrangle, Wyoming, Article 348: U.S. Geological Survey Professional Paper 424-D, p. D170–D173.
- Demaison, G.J., and Moore, G.T., 1980, Anoxic environments and oil source bed genesis: Organic Geochemistry, v. 2, p. 9–31, https://doi.org/10.1016/0146-6380(80)90017-0.
- Demicco, R.V., and Lowenstein, T.K., 2020, When "evaporites" are not formed by evaporation: The role of temperature and pCO₂ on saline deposits of the Eocene Green River Formation, Colorado, USA: Geological Society of America Bulletin, v. 132, p. 1365–1380, https://doi.org/10.1130/B35303.1.
- Doebbert, A.C., Johnson, C.M., Carroll, A.R., Beard, B.L., Pietras, J.T., Rhodes Carson, M., Norsted, B., and Throckmorton, L.A., 2014, Controls on Sr isotopic evolution in lacustrine systems: Eocene green river formation, Wyoming: Chemical Geology, v. 380, p. 172–189, https://doi.org/10.1016/j.chemgeo.2014.04.008.
- Dyer-Pietras, K.M., 2020, Insolation forcing of sub-lacustrine debris flows—Could monsoon intensification have played a role? Eocene lacustrine Green River Formation, Piceance Creek Basin, Colorado: Palaeogeography, Palaeoclimatology, Palaeoecology, v. 553, https://doi.org/10.1016/j.palaeo.2020.109738.
- Dyni, J.R., 1974, Stratigraphy and nahcolite resources of the saline facies of the Green River Formation, Rio Blanco County, Colorado: U.S. Geological Survey Open-File Report 74-56, 28 p.

- Dyni, J.R., 1976, Trioctahedral smectite in the Green River Formation, Duchesne County, Utah: U.S. Geological Survey Professional Paper 967, 14 p., https://doi.org/10.3133/pp967.
- Dyni, J.R., 1997, Sodium carbonate resources of the Green River Formation in Utah, Colorado, and Wyoming: U.S. Geological Survey Open-File Report 96-729, 39 p.
- Dyni, J.R., Wiig, S.V., and Grundy, W.D., 1995, Trona resources in southwest Wyoming: Natural Resources Research, v. 4, p. 340–352.
- Eugster, H.P., and Hardie, L.A., 1975, Sedimentation in an ancient playa-lake complex: The Wilkins Peak Member of the Green River Formation of Wyoming: Geological Society of America Bulletin, v. 86, p. 319–334, https://doi.org/10.1130/0016-7606(1975)86<319:SIAAPC>2 .0.CO:2.
- Fischer, A.G., and Roberts, L.T., 1991, Cyclicity in the Green River Formation (lacustrine Eocene) of Wyoming: Journal of Sedimentary Petrology, v. 61, p. 1146–1154.
- Hansen, W.R., 1986, History of faulting in the eastern Uinta Mountains, Colorado and Utah, in Stone, D.S., and Johnson K.S., New Interpretations of Northwest Colorado Geology: Rocky Mountain Association of Geologists, 1986 Symposium, p. 5–17.
- Hendrix, M.S., Graham, S.A., Carroll, A.R., Sobel, E.R., McKnight, C.L., Schulein, B.J., and Wang, Z., 1992, Sedimentary record and climatic implications of recurrent deformation in the Tian Shan: Evidence from Mesozoic strata of the north Tarim, south Junggar, and Turpan basins, northwest China: Geological Society of America Bulletin, v. 104, p. 53–79, https://doi.org/10.1130/0016-7606(1992)104<0053:SRACIO>2, 3.CO;2.
- Higley, D.K., 1983, Distribution of bromine in bedded halite in the Green River Formation, southwestern Wyoming: U.S. Geological Survey Open-File Report 83-726, 52 p.
- Hosterman, J.W., and Dyni, J.R., 1972, Clay mineralogy of the Green River Formation, Piceance Creek Basin— A preliminary study, in Geological Survey Research 1972: U.S. Geological Survey Professional Paper 800-D, p. D159–D163.
- Hutchinson, G.E., 1957, A Treatise on Limnology, Volume1: Geography, Physics and Chemistry: New York, John Wiley and Sons, 1015 p.
- Imai, N., Terashima, S., Itoh, S., and Ando, A., 1995, Compilation of analytical data for minor and trace elements in seventeen GSJ geochemical reference samples: Geostandards Newsletter, v. 19, p. 135–213, https://doi.org/10.1111/j.1751-908X.1995.tb00158.x.
- Jagniecki, E.A., Jenkins, D.M., Lowenstein, T.K., and Carroll, A.R., 2013, Experimental study of shortite (Na₂Ca₂(CO₃)₃) formation and application to the burial history of the Wilkins Peak Member, Green River Basin, Wyoming, USA: Geochimica et Cosmochimica Acta, v. 115, p. 31–45, https://doi.org/10.1016/j.gca .2013.04.005.
- Jagniecki, E., and Lowenstein, T., 2015, Evaporites of the Green River Formation, Bridger and Piceance Creek Basins: Deposition, diagenesis, paleobrine chemistry, and Eocene atmospheric CO₂, in Smith, M., and Carroll, A., eds., Stratigraphy and Paleolimnology of the Green River Formation, Western USA: Syntheses in Limnogeology, Volume 1: Dordrecht, Springer, p. 277–312, https://doi.org/10.1007/978-94-017-9906-5_11.
- Johnson, R.C., 1981, Stratigraphic evidence for a deep Eocene Lake Uinta, Piceance Creek Basin, Colorado: Geology, v. 9, p. 55–62, https://doi.org/10.1130 /0091-7613(1981)9<55:SEFADE>2.0.CO;2.
- Johnson, T.C., 1984, Sedimentation in Large Lakes: Annual Review of Earth and Planetary Sciences, v. 12, p. 179–204, https://doi.org/10.1146/annurev.ea.12 .050184.001143.
- Kelts, K., 1988, Environments of deposition of lacustrine petroleum source rocks, in Fleet, A.J., Kelts, K., and Talbot, M.R., eds., Lacustrine Petroleum Source Rocks: An introduction: Geological Society, London, Special Publication 40, p. 3–26, https://doi.org/10.1144/GSL .SP.1988.040.01.02.
- Kiro, Y., Goldstein, S.L., Lazar, B., and Stein, M., 2016, Environmental implications of salt facies in the Dead

- Sea: Geological Society of America Bulletin, v. 128, p. 824–841, https://doi.org/10.1130/B31357.1.
- Klonowski, E., Lowenstein, T.K., Carroll, A.R., Smith, M.E., Paperini, M., and Pietras, J.T., 2022, Recurring lacustrine depositional successions in the Wilkins Peak Member, Green River Formation: The basin-center evaporite perspective: Utah Geological Association Publication, v. 50, 23 p.
- Lensky, N.G., Dvorkin, Y., Lyakhovsky, V., Gertman, I., and Gavrieli, I., 2005, Water, salt, and energy balances of the Dead Sea: Water Resources Research, v. 41, https:// doi.org/10.1029/2005WR004084.
- Lowenstein, T.K., Weldeghebriel, M.F., Sirota, I., Eyal, H., Mor, Z., Lensky, N.G., and Lokier, S., 2021, Criteria for the recognition of clastic halite: The modern Dead Sea shoreline: Sedimentology, v. 68, p. 2253–2269, https:// doi.org/10.1111/sed.12907.
- Machlus, M.L., Olsen, P.E., Christie-Blick, N., and Hemming, S.R., 2008, Spectral analysis of the lower Eocene Wilkins Peak Member, Green River Formation, Wyoming: Support for Milankovitch cyclicity: Earth and Planetary Science Letters, v. 268, p. 64–75, https://doi.org/10.1016/j.epsl.2007.12.024.
- Machlus, M.L., Ramezani, J., Bowring, S.A., Hemming, S.R., Tsukui, K., and Clyde, W.C., 2015, A strategy for cross-calibrating U-Pb chronology and astrochronology of sedimentary sequences: An example from the Green River Formation, Wyoming, USA: Earth and Planetary Science Letters, v. 413, p. 70–78, https://doi .org/10.1016/j.epsl.2014.12.009.
- Mason, G.M., 1987, Mineralogic aspects of stratigraphy and geochemistry of the Green River Formation, Wyoming [Ph.D. thesis]: Laramie, The University of Wyoming, 377 p.
- Meyers, S.R., 2008, Resolving Milankovitchian controversies: The Triassic Latemar Limestone and the Eocene Green River Formation: Geology, v. 36, p. 319–322, https://doi.org/10.1130/G24423A.1.
- Meyers, S.R., 2014, Astrochron: An R package for Astrochronology: https://cran.r-project.org/package=astrochron.
- Meyers, S.R., Sageman, B.B., and Hinnov, L.A., 2001, Integrated quantitative stratigraphy of the Cenomanian—Turonian Bridge Creek Limestone Member using evolutive harmonic analysis and stratigraphic modeling: Journal of Sedimentary Research, v. 71, p. 628–644, https://doi.org/10.1306/012401710628.
- Meyers, S.R., Sageman, B.B., and Pagani, M., 2008, Resolving Milankovitch: Consideration of signal and noise: American Journal of Science, v. 308, p. 770–786, https://doi.org/10.2475/06.2008.02.
- Mingram, J., 1998, Laminated Eocene maar-lake sediments from Eckfeld (Eifel region, Germany) and their shortterm periodicities: Palaeogeography, Palaeoclimatology, Palaeoecology, v. 140, p. 289–305, https://doi.org /10.1016/S0031-0182(98)00021-2.
- Olson, K.J., and Lowenstein, T.K., 2021, Searles Lake evaporite sequences: Indicators of late Pleistocene/Holocene lake temperatures, brine evolution, and pCO₂: Geological Society of America Bulletin, v. 133, p. 2319–2334, https://doi.org/10.1130/B35857.1.
- Picard, M.D., and High, L.R., 1972, Paleoenvironmental reconstructions in an area of rapid facies change, Parachute Creek Member of Green River Formation (Eocene), Uinta Basin, Utah: Geological Society of America Bulletin, v. 83, no. 9, p. 2689–2708, https://doi.org/10.1130/0016-7606(1972)83[2689:PRIAAO]2.0.CO:2.
- Pietras, J.T., and Carroll, A.R., 2006, High-resolution stratigraphy of an underfilled lake basin: Wilkins Peak Member, Eocene Green River Formation, Wyoming, U.S.A.: Journal of Sedimentary Research, v. 76, p. 1197–1214, https://doi.org/10.2110/jsr.2006.096.
- Pietras, J.T., Carroll, A.R., Singer, B.S., and Smith, M.E., 2003a, 10 k.y. depositional cyclicity in the early Eocene: Stratigraphic and ⁴⁰ArJ⁵⁹Ar evidence from the lacustrine Green River Formation: Geology, v. 31, p. 593–596, https://doi.org/10.1130 /0091-7613(2003)031<0593:KDCITE>2.0.CO;2.
- Pietras, J.T., Carroll, A.R., and Rhodes, M.K., 2003b, Lake basin response to tectonic drainage diversion: Eocene Green River Formation, Wyoming: Journal of Paleo-

- limnology, v. 30, p. 115–125, https://doi.org/10.1023/A:1025518015341.
- R Core Team, 2021, R: A Language and Environment for Statistical Computing: Vienna, Austria, R Foundation for Statistical Computing.
- Robb, W.A., and Smith, J.W., 1974, Mineral profile of the oil shales in Colorado core hole no. 1, Piceance Creek Basin, Colorado, in Keith Murray, D., ed., Guidebook to the Energy Resources of the Piceance Creek Basin Colorado: Rocky Mountain Association of Geologists Twenty-Fifth Field Conference Guidebook, p. 91–100.
- Roehler, H.W., 1992, Correlation, composition, areal distribution, and thickness of Eocene stratigraphic units, greater Green River Basin, Wyoming, Utah, and Colorado: U.S. Geological Survey Professional Paper Report 1506E, 49 p., http://pubs.er.usgs.gov/publication/pp1506E.
- Roehler, H.W., 1993, Eocene climates, depositional environments, and geography, greater Green River Basin, Wyoming, Utah, and Colorado: U.S. Geological Survey Professional Paper 1506-F, 74 p.
- Sageman, B.B., and Hollander, D.J., 1999, Integration of paleoecological and geochemical proxies: A holistic approach to the study of past global change, in Johnson, C.J., and Barrera, E., eds., The Evolution of Cretaceous Ocean/Climate Systems: Geological Society of America Special Paper 332, p. 365–384, https://doi.org /10.1130/0-8137-2332-9.365.
- Sears, J.W., Graff, P.J., and Holden, G.S., 1982, Tectonic evolution of lower Proterozoic rocks, Uinta Mountains, Utah and Colorado: Geological Society of America Bulletin, v. 93, p. 990–997, https://doi.org/10 .1130/0016-7606(1982)93<990:TEOLPR>2.0.CO;2.
- Sheriff, S.D., and Shive, P.N., 1982, Unreliable paleomagnetic results from the Wilkins Peak Member of the Eocene Green River Formation, Wyoming: Geophysical Research Letters, v. 9, p. 723–726, https://doi.org/10.1029/GL009i006p00723.
- Sirota, I., Arnon, A., and Lensky, N.G., 2016, Seasonal variations of halite saturation in the Dead Sea: Water Resources Research, v. 52, p. 7151–7162, https://doi.org/10.1002/2016WR018974.
- Sirota, I., Enzel, Y., and Lensky, N.G., 2017, Temperature seasonality control on modern halite layers in the Dead Sea: In situ observations: Geological Society of America Bulletin, v. 129, p. 1181–1194, https://doi.org/10 .1130/B31661.1.
- Smith, M.E., and Carroll, A.R., 2015, Introduction to the Green River Formation, in Smith, M., and Carroll, A., eds., Stratigraphy and Paleolimnology of the Green River Formation, Western USA: Syntheses in Limnogeology, Volume 1: Dordrecht, Springer, p. 1–12, https:// doi.org/10.1007/978-94-017-9906-5_1.
- Smith, M.E., Singer, B.S., and Carroll, A.R., 2003, ⁴⁰Ar/³⁹Ar geochronology of the Eocene Green River Formation, Wyoming: Geological Society of America Bulletin, v. 115, p. 549–565, https://doi.org/10.1130 //0016-7606(2003)115<0549:AGOTEG>2.0.CO:2.
- Smith, M.E., Carroll, A.R., and Singer, B.S., 2008, Synoptic reconstruction of a major ancient lake system: Eocene Green River Formation, western United States: Geological Society of America Bulletin, v. 120, p. 54–84, https://doi.org/10.1130/B26073.1.
- Smith, M.E., Chamberlain, K.R., Singer, B.S., and Carroll, A.R., 2010, Eocene clocks agree: Coeval ⁴⁰Ar/³⁹Ar, U-Pb, and astronomical ages from the Green River Formation: Geology, v. 38, no. 6, p. 527–530, https:// doi.org/10.1130/G30630.1.
- Smith, M.E., Carroll, A.R., Jicha, B.R., Cassel, E.J., and Scott, J.J., 2014a, Paleogeographic record of Eocene Farallon slab rollback beneath western North America: Geology, v. 42, p. 1039–1042, https://doi.org/10.1130 //G36025.1.
- Smith, M.E., Carroll, A.R., Scott, J.J., and Singer, B.S., 2014b, Early Eocene carbon isotope excursions and landscape destabilization at eccentricity minima: Green River Formation of Wyoming: Earth and Planetary Science Letters, v. 403, p. 393–406, https://doi.org/10 .1016/j.epsl.2014.06.024.
- Smith, M.E., Carroll, A.R., and Scott, J.J., 2015, Stratigraphic expression of climate, tectonism, and

Walters et al.

- geomorphic forcing in an underfilled lake basin: Wilkins Peak Member of the Green River Formation, *in* Smith, M., and Carroll, A., Stratigraphy and Paleolimnology of the Green River Formation, Western USA: Dordrecht, Springer, p. 61–102, https://doi.org/10.1007/978-94-017-9906-5_4.
- Smoot, J.P., 1983, Depositional subenvironments in an arid closed basin; the Wilkins Peak Member of the Green River Formation (Eocene), Wyoming, USA: Sedimentology, v. 30, p. 801–827, https://doi.org/10.1111/j .1365-3091.1983.tb00712.x.
- South African Committee for Certified Reference Materials, 1990, Catalogue of Certified Reference Materials: South Africa Bureau of Standards, 36 p.
- Sullivan, R., 1980, A stratigraphic evaluation of the Eocene rocks of southwestern Wyoming: The Geological Survey of Wyoming Report of Investigations 20, p. 1–50.
- Surdam, R.C., and Stanley, K.O., 1980, Effects of changes in drainage-basin boundaries on sedimentation in Eocene Lakes Gosiute and Uinta of Wyoming, Utah, and Colorado: Geology, v. 8, p. 135–139, https://doi.org/10.1130/0091-7613(1980)8<135:EOCIDB>2.0.CO:2.
- Tänavsuu-Milkeviciene, K., and Sarg, J.F., 2012, Evolution of an organic-rich lake basin—stratigraphy, climate and tectonics: Piceance Creek Basin, Eocene Green River Formation: Evolution of an organic-rich lake: Sedimen-

- tology, v. 59, p. 1735–1768, https://doi.org/10.1111/j.1365-3091.2012.01324.x.
- Tänavsuu-Milkeviciene, K., Sarg, J.F., and Bartov, Y., 2017, Depositional cycles and sequences in an organic-rich lake basin: Eocene Green River Formation, Lake Uinta, Colorado and Utah, U.S.A.: Journal of Sedimentary Research, v. 87, p. 210–229, https://doi.org/10.2110/ isr.2017.11.
- Thomson, D.J., 1982, Spectrum estimation and harmonic analysis: Proceedings of the IEEE, v. 70, p. 1055–1096, https://doi.org/10.1109/PROC.1982.12433.

 Vanden Berg, M.D., and Birgenheier, L.P., 2017, An exami-
- Vanden Berg, M.D., and Birgenheier, L.P., 2017, An examination of the hypersaline phases of Eocene Lake Uinta, upper Green River Formation, Uinta Basin, Utah: Journal of Paleolimnology, v. 58, p. 353–371, https://doi.org/10.1007/s10933-017-9983-x.
- Walters, A.P., Meyers, S.R., Carroll, A.R., Hill, T.R., and Vanden Berg, M.D., 2020, Lacustrine cyclicity in the early Eocene Green River Formation, Uinta Basin, Utah: Evidence from X-ray fluorescence core scanning: Journal of Sedimentary Research, v. 90, p. 429–447, https://doi.org/10.2110/jsr.2020.24.
- Westerhold, T., and Röhl, U., 2009, High resolution cyclostratigraphy of the early Eocene—new insights into the origin of the Cenozoic cooling trend: Climate of the Past, v. 5, p. 309–327, https://doi.org/10.5194/cp-5-309-2009.
- Westerhold, T., Röhl, U., Donner, B., and Zachos, J.C., 2018, Global extent of early Eocene hyperthermal events: A

- new Pacific benthic foraminiferal isotope record from Shatsky Rise (ODP Site 1209): Paleoceanography and Paleoclimatology, v. 33, p. 626–642, https://doi.org/10.1029/2017PA003306.
- Wiig, S.V., Grundy, W.D., and Dyni, J.R., 1995, Trona resources in the Green River basin, southwest Wyoming: U.S. Geological Survey Open-File Report 95-476, 88 p.
- Zachos, J., Pagani, M., Sloan, L., Thomas, E., and Billups, K., 2001, Trends, rhythms, and aberrations in global climate 65 Ma to present: Science, v. 292, p. 686–693, https://doi.org/10.1126/science.1059412.
- Zachos, J.C., Dickens, G.R., and Zeebe, R.E., 2008, An early Cenozoic perspective on greenhouse warming and carbon-cycle dynamics: Nature, v. 451, p. 279–283, https://doi.org/10.1038/nature06588.
- Zeebe, R.E., Westerhold, T., Littler, K., and Zachos, J.C., 2017, Orbital forcing of the Paleocene and Eocene carbon cycle: Paleoceanography and Paleoclimatology, v. 32, p. 440–465, https://doi.org/10.1002/2016PA003054.

SCIENCE EDITOR: WENJIAO XIAO ASSOCIATE EDITOR: CHRISTIAN KOEBERL

MANUSCRIPT RECEIVED 29 APRIL 2022 REVISED MANUSCRIPT RECEIVED 29 AUGUST 2022 MANUSCRIPT ACCEPTED 7 OCTOBER 2022

Printed in the USA